JM PAPERS

The sub-microscale dynamics of double-diffusive convection

Timour Radko†

Department of Oceanography, Naval Postgraduate School, Monterey, CA 93943, USA

This study investigates the dynamics of fingering convection on scales much smaller than the typical size of individual salt fingers. On such scales, salinity patterns exhibit the spontaneous emergence of sharp fronts induced by finger-scale strain. In contrast, velocity and temperature fields are largely devoid of sub-microscale variability, which is attributed to the rapid molecular dissipation of heat and momentum. The presence of fine salinity structures fundamentally limits the efficiency of direct numerical simulations (DNS) of double-diffusive processes. In the oceanographic context, the computational cost of resolving sub-microscale salinity features exceeds that of temperature-only DNS by up to four orders of magnitude, severely restricting the types of double-diffusive systems that can be studied numerically. To address this complication, we introduce the sub-microscale filtering (SMF) algorithm, which resolves temperature and velocity while parameterizing the sub-microscale dynamics of salinity. The proposed closure draws inspiration from the Smagorinsky scheme, which represents unresolved processes by the downgradient strain-dependent momentum flux. The SMF model is successfully validated through fully resolved simulations.

Key words: double diffusive convection

1. Introduction

The term double-diffusive convection represents a wide range of processes that are driven by unequal diffusivities of properties affecting fluid density. Following the seminal discovery of primary double-diffusive instabilities (Stern 1960), investigations of multi-component flows evolved into a distinct and vibrant branch of fluid mechanics. Double-diffusive phenomena have been studied most extensively in the oceanographic context (Schmitt 1994; Kelley *et al.* 2003; Radko 2013), where the density of seawater is controlled by its temperature and salinity. Since heat diffuses approximately a hundred times faster than salt, double-diffusive processes in the ocean tend to be intense and

† Email address for correspondence: tradko@nps.edu

widespread (You 2002). In several critical regions, they dominate the vertical mixing of water masses (Schmitt *et al.* 2005; Guthrie, Fer, & Morison 2015), motivating in-depth studies of double-diffusive dynamics and transport. The fingering mode of double-diffusive convection is particularly common in the main thermocline, a stratified region extending from the base of the surface mixed layer to depths of approximately one kilometre. In the Atlantic Ocean, at least 90% of the main thermocline is fingering favourable (Schmitt 1994). In addition to oceanic systems, double-diffusive convection is also realized – and plays a significant role – in numerous astrophysical, geophysical and engineering applications (e.g. Turner 1985; Radko 2013; Garaud 2018).

In the spirit of the times, much recent progress in understanding double-diffusive convection has been brought by numerical modelling (e.g. Smyth & Kimura 2011; Hieronymus & Carpenter 2016; Yang, Verzicco & Lohse 2016, 2020; Ouillon *et al.* 2020; Ma & Peltier 2021; Brown & Radko 2022). However, the principal limitation of such efforts lies in the prohibitive computational cost of modelling many realistic configurations. Double-diffusive processes are initiated by molecular diffusion and therefore primary instabilities in seawater operate on spatial scales of centimetres, placing them in the category of oceanic microstructure. While interesting in their own right, an even broader geophysical significance of primary double-diffusive instabilities lies in their ability to induce much larger flows. This dynamics is exemplified by salt fingers, the vertically elongated microscale filaments that form in the ocean regions where temperature and salinity increase upward. Salt fingers frequently induce secondary circulation patterns, which include lateral intrusions (Stern 1967; Ruddick & Kerr 2003; Ruddick & Richards 2003), collective instability waves (Stern 1969; Stern, Radko & Simeonov 2001) and thermohaline staircases (Stern & Turner 1969; Stellmach *et al.* 2011). The spatial extents of these secondary double-diffusive patterns exceed the scale of individual fingers by at least 2–3 orders of magnitude, which presents a fundamental obstacle for numerical models. Despite continuous advancements in high-performance computing, microstructure-resolving simulations of double-diffusive processes are still extremely demanding. Even with a major investment of computational resources, users are often forced to make painful concessions in terms of the realism of model configurations and chosen parameters. Several models attempted to parameterize, rather than resolve, double-diffusive microstructure (e.g. Stern & Simeonov 2002; Simeonov & Stern 2004; Radko & Sisti 2017). The latter approach, however, suffers from uncertainties in the formulation of such parameterizations and is expected to provide only qualitative descriptions of the processes at play.

Yet another modelling challenge – and the one that the present study strives to address – stems from the difference in the molecular diffusivities of heat and salt, k_T and k_S, respectively. The dissipation scale of salinity is less than the dissipation scale of temperature by a factor of $\sqrt{k_T k_S^{-1}} \sim 10$ (e.g. Radko 2008), which conforms to the Batchelor (1959) scaling of scalar dissipation. Thus, the requirement to resolve sub-microscale salinity features increases the computational cost by a factor of 10^3 in two-dimensional (2-D) simulations and 10^4 in three dimensions relative to the investment in equivalent temperature-only direct numerical simulations (DNS). Unfortunately, this complication makes several fundamental double-diffusive problems numerically inaccessible even in two dimensions. Note that the difference in diffusivities captures the very essence of double diffusion and therefore it must be reflected in any meaningful simulations. Many earlier numerical studies reduced the associated computational burden by considering the salt/heat diffusivity ratios $\tau \equiv k_S k_T^{-1}$ that are much larger than the

oceanic value of $\tau \sim 0.01$ (e.g. Stern *et al.* 2001; Kimura, Smyth, & Kunze 2011; Brown & Radko 2022). While acceptable for preliminary explorations, concerns regarding the ability of such models to accurately represent oceanic processes call for a more cardinal solution to the problem. Another approach involves using a much finer mesh for salinity than for temperature and velocity (e.g. Kimura *et al* 2011; Smyth & Kimura 2011). However, since the fine mesh must still resolve the salinity dissipation scale, this technique reduces the computational cost by less than a factor of five. Thus, while the advent of double-grid DNS represents a welcome addition to the modelling toolbox, many double-diffusive problems remain numerically inaccessible.

This study addresses the twin challenges of explaining the sub-microscale dynamics of double-diffusive convection and offering a physics-based representation of key processes that can be implemented in coarse-resolution numerical models. The formation of the sub-microscale salinity patterns is attributed to the strain by the finger-scale velocity field, which stretches the salinity filaments and systematically reduces their effective width. The resulting direct cascade of salinity variance is arrested only at scales that are small enough to be effectively damped by the molecular dissipation of salt. This chain of events is consistent with the classical description of the small-scale behaviour of weakly diffusive scalars in the presence of turbulence by Batchelor (1959). To capture this dynamics, we develop a strain-dependent subgrid salinity model. This closure is inspired by the pioneering large eddy simulation (LES) approach of Smagorinsky (1963), where an analogous scheme was implemented to parameterize the subgrid momentum transfer. In contrast, the present algorithm targets salinity and makes no attempt to parameterize momentum and temperature, which are fully resolved. This sub-microscale filtering (SMF) model is used to simulate fingering convection in the oceanographically relevant regime and is validated by the corresponding salinity-resolving experiments.

The material is organized as follows. The governing equations are described in § 2. Section 3 presents the physical arguments and supporting simulations that establish the link between the sub-microscale salinity dissipation and the finger-scale velocity strain. Section 4 introduces the strain-based subgrid model of salinity. We validate the SMF model using fully resolved 2-D and 3-D simulations in §§ 5 and 6, respectively. The results are summarized, and conclusions are drawn, in § 7.

2. Formulation

To explore the circulation patterns in an effectively unbounded doubly stratified fluid, the total temperature and salinity fields (T_{tot}^*, S_{tot}^*) are separated into the background state (T_{bg}^*, S_{bg}^*), representing uniform vertical gradients, and a departure (T^*, S^*) from them:

$$\left.\begin{aligned} T_{tot}^* = T_{bg}^* + T^* = A_T z^* + A_{T0} + T^*, \\ S_{tot}^* = S_{bg}^* + S^* = A_S z^* + A_{S0} + S^*, \end{aligned}\right\} \tag{2.1}$$

where $(A_T, A_{T0}, A_S, A_{S0})$ are constants and the asterisks denote dimensional field variables. Our focus is on finger-favourable stratification, where $\partial T_{bg}^*/\partial z^* = A_T > 0$ and $\partial S_{bg}^*/\partial z^* = A_S > 0$. We ignore planetary rotation, compressibility and the nonlinearity of the equation of state and express the governing Boussinesq equations in terms of

perturbations (T^*, S^*):

$$
\left.
\begin{aligned}
\frac{\partial T^*}{\partial t^*} + \boldsymbol{v}^* \cdot \boldsymbol{\nabla} T^* + A_T w^* &= k_T \nabla^2 T^*, \\
\frac{\partial S^*}{\partial t^*} + \boldsymbol{v}^* \cdot \boldsymbol{\nabla} S^* + A_S w^* &= k_S \nabla^2 S^*, \\
\frac{\partial \boldsymbol{v}^*}{\partial t^*} + \boldsymbol{v}^* \cdot \boldsymbol{\nabla} \boldsymbol{v}^* &= -\frac{1}{\rho_0^*} \boldsymbol{\nabla} p^* + g(\alpha T^* - \beta S^*)\boldsymbol{k} + \upsilon \nabla^2 \boldsymbol{v}^*, \\
\boldsymbol{\nabla} \cdot \boldsymbol{v}^* &= 0,
\end{aligned}
\right\}
\tag{2.2}
$$

where $\boldsymbol{v}^* = (u^*, v^*, w^*)$ is the velocity, $\boldsymbol{k}$ is the vertical unit vector, p^* is the dynamic pressure, g is gravity, (α, β) are the thermal expansion and haline contraction coefficients and ρ_0^* is the reference density.

We adopt the traditional double-diffusive non-dimensionalization (e.g. Radko 2013) based on scales of individual salt fingers. Thus, $l = (k_T \upsilon/g\alpha A_T)^{1/4}$, k_T/l, l^2/k_T and $\rho_0^* \upsilon k_T/l^2$ are used as the units of length, velocity, time and pressure, respectively, whereas temperature and salinity are non-dimensionalized as follows:

$$
T^* = A_T l T, \quad S^* = \frac{\alpha}{\beta} A_T l S. \tag{2.3a,b}
$$

After non-dimensionalization, the governing equations are reduced to

$$
\left.
\begin{aligned}
\frac{\partial T}{\partial t} + \boldsymbol{v} \cdot \boldsymbol{\nabla} T + w &= \nabla^2 T, \\
\frac{\partial S}{\partial t} + \boldsymbol{v} \cdot \boldsymbol{\nabla} S + \frac{w}{R_\rho} &= \tau \nabla^2 S, \\
\frac{1}{Pr}\left(\frac{\partial}{\partial t}\boldsymbol{v} + \boldsymbol{v} \cdot \boldsymbol{\nabla} \boldsymbol{v}\right) &= -\boldsymbol{\nabla} p + (T - S)\boldsymbol{k} + \nabla^2 \boldsymbol{v}, \\
\boldsymbol{\nabla} \cdot \boldsymbol{v} &= 0,
\end{aligned}
\right\}
\tag{2.4}
$$

where $R_\rho = \alpha A_T/\beta A_S$ is the background density ratio, $\tau = k_S/k_T$ is the diffusivity ratio and $Pr = \upsilon/k_T$ is the Prandtl number. Some calculations in this study are performed in two dimensions (x, z), which reduces the Boussinesq system (2.4) to

$$
\left.
\begin{aligned}
\frac{\partial T}{\partial t} + J(\psi, T) + \frac{\partial \psi}{\partial x} &= \nabla^2 T, \\
\frac{\partial S}{\partial t} + J(\psi, S) + \frac{1}{R_\rho}\frac{\partial \psi}{\partial x} &= \tau \nabla^2 S, \\
\frac{\partial}{\partial t}\nabla^2 \psi + J(\psi, \nabla^2 \psi) &= Pr\left[\frac{\partial}{\partial x}(T - S) + \nabla^4 \psi\right],
\end{aligned}
\right\}
\tag{2.5}
$$

where ψ is the streamfunction associated with the velocity field $(u, w) = (-\partial\psi/\partial z, \partial\psi/\partial x)$, and $J(a, b) \equiv (\partial a/\partial x)(\partial b/\partial z) - (\partial a/\partial z)(\partial b/\partial x)$ is the Jacobian.

3. Sub-microscale dynamics of double-diffusive convection

To illustrate the key features of fingering convection, we present a typical 2-D DNS. The governing equations (2.5) are integrated in time using the Fourier-based spectral model (e.g. Stern *et al.* 2001; Radko 2019*a*) with periodic boundary conditions assumed
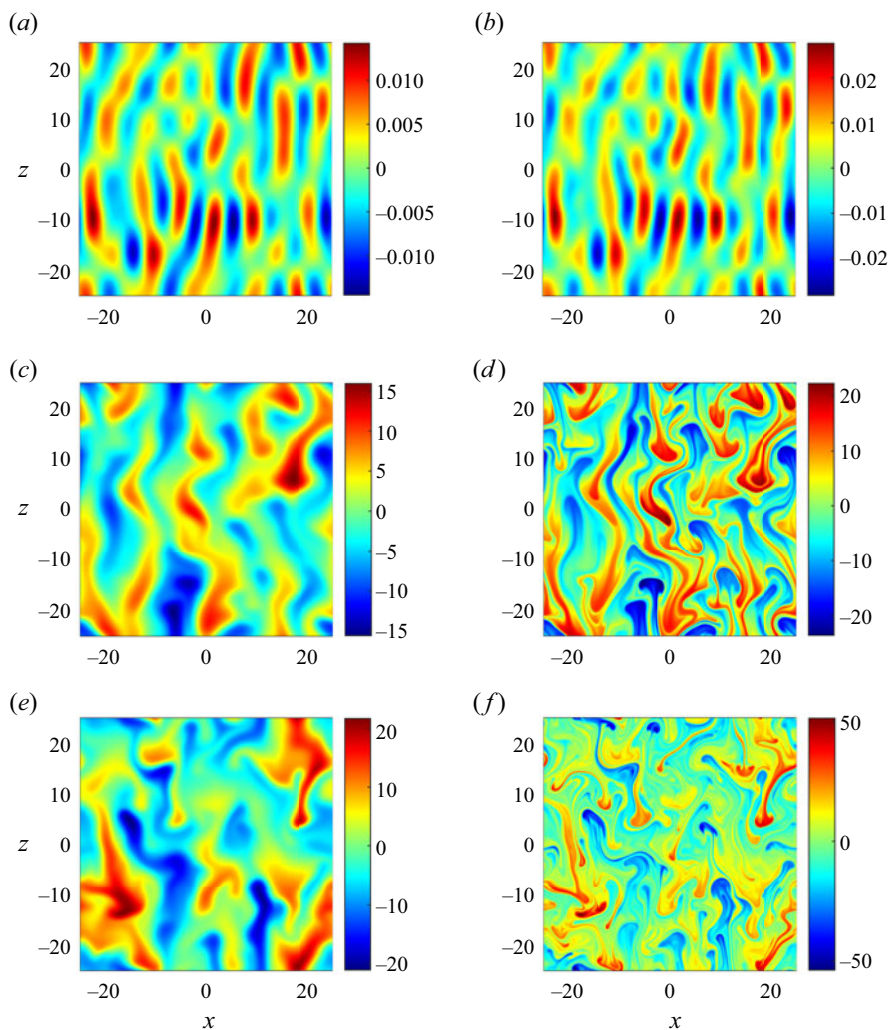
Figure 1. Salt finger DNS performed with $(Pr, \tau, R_\rho) = (7, 0.01, 2)$. The instantaneous patterns of temperature (left panels) and salinity (right panels) are shown for (a,b) $t = 20$, (c,d) $t = 50$ and (e,f) $t = 100$.

for (ψ, T, S) in each direction. The periodicity of perturbations reflects the effectively unbounded character of double diffusion in the ocean. Salt fingers are most common at depths of several hundred metres and therefore are unaffected by the surface and sea-floor boundaries. The unbounded model of double diffusion has been validated by oceanic observations. The most recent and comprehensive analysis performed for a wide range of environmental conditions (Brown & Radko 2024) unambiguously confirmed the model's ability to represent field measurements and the lack of systematic biases.

The calculation in figure 1 was performed with the oceanographically relevant (e.g. Radko 2013) values of governing parameters $(Pr, \tau, R_\rho) = (7, 0.01, 2)$ on the computational domain of size $L_x \times L_z = 50 \times 50$, resolved by $(N_x, N_z) = (2048, 2048)$ grid points. The experiment was initiated by the random low-amplitude distribution of (ψ, T, S), introduced to seed primary instabilities. The experiment is extended for $t = 1000$ time units – dimensionally equivalent to 10 days for oceanic scales. The first stage
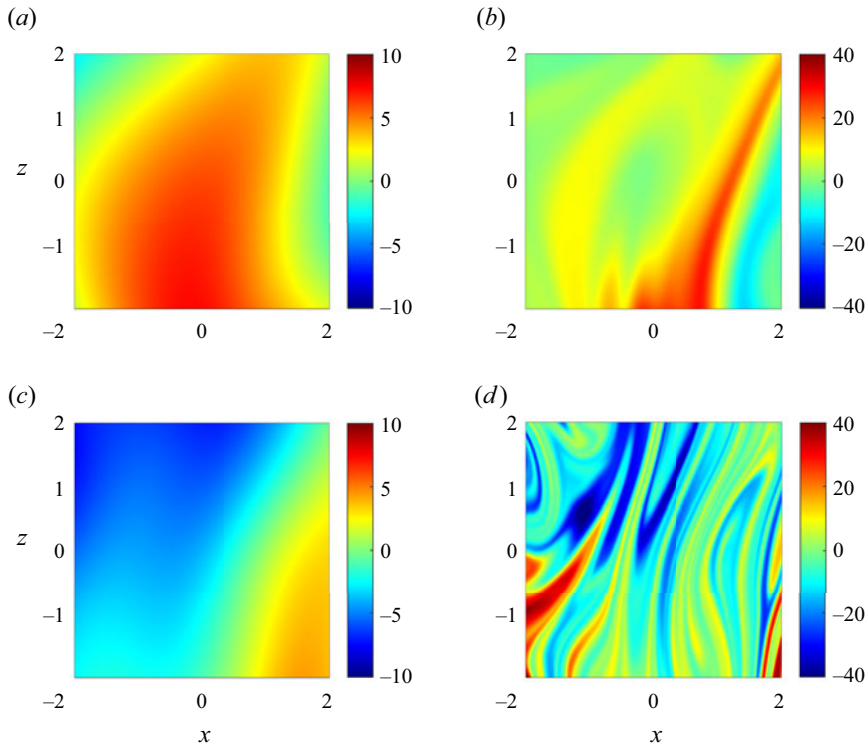
Figure 2. The magnified view of temperature (*a*) and salinity (*b*) in the small area Ω for the state in figure 1(*e*,*f*). Panels (*c*) and (*d*) show the corresponding patterns realized in the analogous experiment performed with $\tau = 5 \times 10^{-4}$ at $t = 100$. Note the emergence of numerous sub-microscale fronts of salinity in (*d*).

in the development of instability is marked by the spontaneous emergence of vertically oriented salt fingers. The temperature and salinity patterns, shown in figure 1(*a*,*b*) at $t = 20$, are relatively regular and vary on comparable spatial scales. However, by $t = 50$, primary salt fingers develop secondary instabilities (e.g. Radko & Smith 2012) and the flow field becomes more turbulent and disorganized (figure 1*c*,*d*). The statistical equilibration of salt fingers is completed by $t = 100$ (figure 1*e*,*f*). Afterward, the quasi-steady state is maintained indefinitely.

A salient feature of the resulting solutions is the emergence of fine structures in the salinity field that are not reflected in the corresponding temperature and velocity patterns. To better illustrate this phenomenon, we present (figure 2*a*,*b*) a magnified view of *T* and *S* over a small area of

$$\Omega = \{-2 < x < 2, \ -2 < z < 2\}. \tag{3.1}$$

The sub-microscale salinity patterns appear in the form of narrow fronts and their width is controlled by the molecular dissipation of salt. The latter assumption is readily confirmed by reproducing the simulation in figure 1 with a much lower diffusivity ratio of $\tau = 5 \times 10^{-4}$ (figure 2*c*,*d*). To fully resolve the 'salinity' spectrum, we employ a finer mesh with $(N_x, N_z) = (4096, 4096)$ grid points. The resulting salinity pattern (figure 2*d*) is characterized by even narrower and more tightly packed fronts than in the baseline experiment (figure 2*b*). This dynamics conforms to the view expressed by Batchelor (1959), who attributed the fine features of weakly diffusive tracers to larger-scale strain.

982 A25-6

Further insight into the origin of these sub-microscale structures is provided by the salinity variance equation:

$$\frac{\partial}{\partial t}\langle S^2 \rangle + \frac{2}{R_\rho}\langle wS \rangle = -\chi, \tag{3.2}$$

where angle brackets denote spatial averages and $\chi \equiv 2\tau\langle|\nabla S|^2\rangle$. Equation (3.2) was obtained by multiplying the salinity equation in (2.5) by S and averaging the result in x and z. In statistically steady configurations, as considered in our study, the variance production term $\Pi = (2/R_\rho)\langle wS \rangle$ is balanced by the molecular dissipation $(-\chi)$. This so-called production–dissipation balance (Osborn & Cox 1972) concisely describes the link between the large-scale stirring of the salinity field represented by the Π-term and the molecular dissipation on small scales (χ-term). It is also instructive to examine the production–dissipation balance for very low diffusivity ratios. In the limit $\tau \to 0$, the magnitude of the production term approaches a finite value (e.g. Radko 2008), demanding that $|\chi| = O(1)$. This, in turn, requires salinity gradients $|\nabla S| \sim \sqrt{\chi/2\tau} = O(\tau^{-0.5})$ to increase without bound with decreasing τ. The amplification of salinity gradients for small diffusivity ratios is spectacularly manifested by the emergence of numerous sub-microscale fronts, clearly visible in figure 2(*d*).

The tendency for the formation of sub-microscale salinity patterns can also be quantified (figure 3) by examining the dissipation spectra $D(\kappa)$ that satisfy

$$\chi = \int D(\kappa)\,\mathrm{d}\kappa, \tag{3.3}$$

where κ is the 2-D wavenumber. The spectra were computed for the baseline experiment performed with $\tau = 0.01$ (figure 3*a*) and for the low-diffusivity experiment based on $\tau = 5 \times 10^{-4}$ (figure 3*b*). In both cases, spectra were averaged in time over the quasi-equilibrium interval $100 < t < 1000$. The DNS results in figure 3 are compared with the canonical Batchelor (1959) spectrum, which in our non-dimensional units takes the form

$$D_B(\kappa) = C_B \tau \chi \sqrt{\frac{Pr}{\varepsilon}}\kappa \exp(-C_B(\kappa\eta_B)^2), \tag{3.4}$$

where ε is the mean non-dimensional dissipation rate of turbulent kinetic energy, $\eta_B = (Pr\,\tau^2\varepsilon^{-1})^{1/4}$, and C_B is the Batchelor constant. The latter was evaluated from the best fit of (3.4) to the numerical data, resulting in $C_B = 4.01$ and $C_B = 3.95$ for the calculations in (*a*) and (*b*), respectively. The estimates of C_B for temperature dissipation by oceanic turbulence (e.g. Dillon & Caldwell 1980; Oakey 1982) suggest that the Batchelor constant is in the range of 3.4–4.1. The consistency of these values with the salinity-based C_B in double-diffusive experiments – which differ in many ways from the more conventional turbulence problems – underscores the remarkable universality of Batchelor's theory of scalar dissipation.

It should be noted, however, that while the DNS spectra conform to the Batchelor model for relatively low wavenumbers, they exhibit more gentle spectral decay at high ones. Such shallow drop-off is better represented by Kraichnan's (1974) model, which accounts for the fluctuations of the strain rate. Overall, however, the general relevance of Batchelor–Kraichnan ideas to the foregoing simulations is undeniable. Of particular interest to our discussion is the link between scalar dissipation and the strain rate espoused by these theories. To further explore this connection, we examine the statistics of the local dissipation $\chi_{loc} \equiv 2\tau|\nabla S|^2$ as a function of the strain rate (s). The strain rate is defined, in
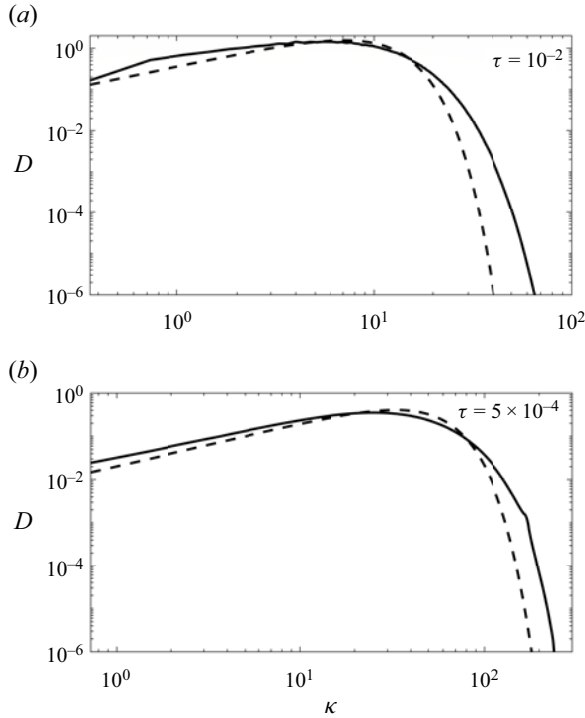
Figure 3. The dissipation spectra for the baseline ($\tau = 0.01$) and low-diffusivity ($\tau = 5 \times 10^{-4}$) simulations are shown by solid curves in (*a*) and (*b*), respectively. The dashed curves represent the corresponding Batchelor (1959) spectra computed as the best fits to the DNS data.

both 2-D and 3-D systems, as

$$s = \sqrt{2s_{ij}s_{ij}}, \quad s_{ij} = \frac{1}{2}\left(\frac{\partial v_i}{\partial x_j} + \frac{\partial v_j}{\partial x_i}\right), \quad (3.5a,b)$$

where

$$(v_1, v_2, v_3) = (u, v, w), \quad (x_1, x_2, x_3) = (x, y, z). \quad (3.6a,b)$$

For each value of strain (s), we estimate the mean dissipation (χ_s) by averaging χ_{loc} over all locations where the strain is in the range $[s - 0.5\Delta s, \ s + 0.5\Delta s]$. In the following calculation, we use $\Delta s = 0.02 \max(s)$ and average the results in time over the quasi-equilibrium interval $100 < t < 1000$.

The $\chi_s(s)$ patterns obtained in this manner for the baseline and low-diffusivity experiments are shown in figure 4. Both simulations reveal a rapid monotonic increase in the dissipation rate with increasing strain. To illustrate the physical mechanisms governing the evolution of sub-microscale variability, we present explicit analytical solutions (Appendix A) that underscore the link between finger-scale strain and the emergence of much finer salinity patterns. We believe that this link captures the essence of the dissipation of salinity in double-diffusive systems, and it should be reflected in any physics-based subgrid closure model, such as described below.
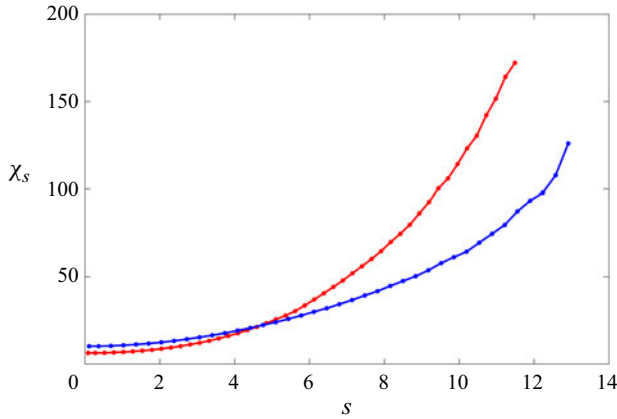
982 A25-8

Figure 4. The mean dissipation rate realized for a given strain is presented for the baseline experiment performed with $\tau = 0.01$ (red curve) and for the low-diffusivity simulation performed with $\tau = 5 \times 10^{-4}$ (blue curve).

4. The SMF model

The simulations of fingering convection reveal the presence of salinity features that are much smaller than those found in the corresponding temperature and momentum fields. Such disparity of scales is the Achilles heel of double-diffusive DNS, which severely limits the scope of numerical investigations in this area and motivates the present effort to develop a subgrid closure for salinity. The proposed algorithm makes no attempt to parameterize momentum and temperature, which are fully resolved, and is referred to as the SMF model.

Our first attempt represented the subgrid transfer of salinity as a Fickian diffusive process with spatially variable eddy diffusivity K:

$$\frac{\partial \bar{S}}{\partial t} + \boldsymbol{v} \cdot \boldsymbol{\nabla} \bar{S} + \frac{w}{R_\rho} = \boldsymbol{\nabla} \cdot (K \boldsymbol{\nabla} \bar{S}) + \frac{\partial}{\partial z} \left(\frac{K}{R_\rho} \right) + \tau \nabla^2 \bar{S}, \tag{4.1}$$

where $\bar{S}$ is the filtered salinity field, and diffusivity K is proportional to the large-scale strain. This subgrid model is analogous to the widely used Smagorinsky (1963) scheme. The key difference is that the original Smagorinsky closure represents the subgrid transfer of momentum. We, on the other hand, are interested solely in modelling the sub-microscale dynamics of salinity.

Closure (4.1) exhibited a reasonably rapid convergence to the corresponding DNS-based solutions with increasing resolution. However, it was subsequently noticed that its bi-harmonic counterpart

$$\frac{\partial \bar{S}}{\partial t} + \boldsymbol{v} \cdot \boldsymbol{\nabla} \bar{S} + \frac{w}{R_\rho} = -\boldsymbol{\nabla} \cdot (K_2 \boldsymbol{\nabla} \bar{S}_2) + \tau \bar{S}_2, \quad \bar{S}_2 = \nabla^2 \bar{S} \tag{4.2}$$

offers a consistently more accurate representation of key mixing characteristics. The coefficient K_2 in (4.2) is parameterized as

$$K_2 = C\delta^4 s, \tag{4.3}$$

where $\delta = L_x/N_x = L_y/N_y = L_z/N_z$ is the grid spacing, and C is an adjustable parameter. The superior performance of the bi-harmonic Smagorinsky closure is attributed to

982 A25-9

its selective suppression of sub-microscale components. The bi-harmonic forcing term in (4.2) has a minimal direct impact on finger-scale components and therefore the model is less invasive and, consequently, more precise. The impact of closure (4.2) on sub-microscale salinity patterns is explored in greater detail in Appendix A, where we use theoretical arguments to rationalize its ability to effectively control grid-scale processes.

An interesting question concerns the choice of the coefficient C in (4.3). A straightforward option – and the one utilized in the Smagorinsky (1963) closure – is a selection of a constant numerical value for C that is applied to all systems considered. More involved are the dynamic models (e.g. Khani & Waite 2015) in which the calibration of subgrid schemes is based on the properties of a particular flow. In the present study, we consider both constant-C and adaptive-C models (§ 5) and find that their accuracy and convergence rates are generally comparable. The selection of the optimal value of C in the adaptive-C closure is based on the requirement to fully resolve the dissipation spectrum of the filtered salinity variance $\bar{D}(\kappa)$. Specifically, we insist that the maximal dissipation $D_{max} = \max_{\kappa} \bar{D}(\kappa)$ significantly exceeds the high-wavenumber dissipation $D_{high} = \max_{\kappa > 0.5\kappa_0} \bar{D}(\kappa)$, where κ_0 is the largest resolved wavenumber. At the same time, we wish to avoid excessive damping of the salinity field. To achieve a reasonable balance between these competing requirements, we assume the target ratio of $D_{max}/D_{high} = 30$. In the course of simulations, C is gradually increased (decreased) when the ratio D_{max}/D_{high} drifts below (above) its target value.

5. Validation: 2-D simulations

All subsequent SMF runs are based on the bi-harmonic Smagorinsky model (4.2) of the salinity field. We start by analysing its performance in two dimensions. An obvious benefit of 2-D simulations is their efficiency, which permits a more systematic exploration of the parameter space. It should also be noted that externally induced large-scale flows, which are ubiquitous in the ocean, favour the formation of salt sheets aligned in the direction of the background shear (Linden 1974; Kimura & Smyth 2007; Radko *et al.* 2015). In such cases, salt fingers become effectively two-dimensional. This tendency implies that analyses based on 2-D models may be more oceanographically relevant.

To illustrate the efficacy of the proposed subgrid closure, we now reproduce the earlier simulations (§ 3) with the SMF model. Equation (4.2) is used to integrate salinity, the original equations in (2.5) are used for temperature and vorticity, and the previously employed spectral code is altered only by including the subgrid forcing term. The key benefit of the SMF model is its ability to perform integrations on much coarser grids. For instance, figure 5 presents the analogue of the simulation in figure 1 performed with only $(N_x, N_z) = (128, 128)$ grid points using the adaptive-C model. This mesh can barely represent the temperature and momentum fields, and most of the original salinity dissipation spectrum (figure 3) is unresolved. Nevertheless, the SMF model offers the description of fingering convection (figure 5) that is consistent with the corresponding fully resolved simulation (cf. figure 1). By $t = 20$, vertically elongated patterns form in both temperature and salinity (figure 5*a,b*). These primary salt fingers gradually amplify and, by $t = 50$ (figure 5*c,d*), develop secondary instabilities, which lead to the statistical equilibration of the flow field. After $t = 100$ (figure 5*e,f*), the system maintains a quasi-steady state.

A more quantitative assessment of the SMF model is afforded by the analysis of kinetic energy (E), as well as turbulent fluxes of heat (F_T), salt (F_S) and density (F_ρ):

$$F_T = \langle wT \rangle, \quad F_S = \langle wS \rangle, \quad F_\rho = \langle w(S - T) \rangle, \quad E = \tfrac{1}{2}\langle v_i v_i \rangle. \qquad (4.4a\text{--}d)$$
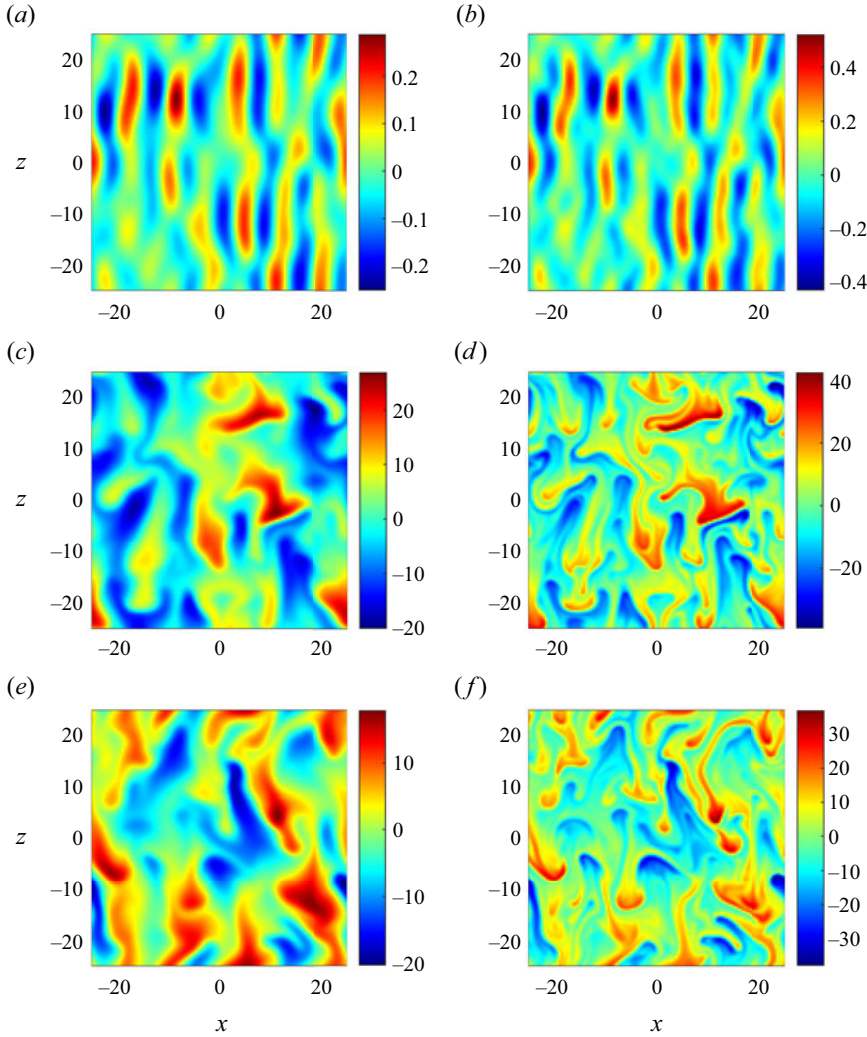
Figure 5. The SMF analogue of the simulation in figure 1. The instantaneous patterns of temperature (left panels) and filtered salinity (right panels) are shown for (a,b) $t = 20$, (c,d) $t = 50$ and (e,f) $t = 100$.

The corresponding expression of the salt flux in terms of filtered salinity is given by

$$F_S = \langle w\bar{S} \rangle - \left\langle K_2 \frac{\partial}{\partial z} \nabla^2 \bar{S} \right\rangle. \tag{4.5}$$

The first term on the right-hand side of (4.5) represents the resolved salt flux, which greatly exceeds the second (parameterized) component in all SMF simulations. The corresponding density flux $F_\rho = F_S - F_T$ is evaluated using (4.5). The prediction of quantities (4.4) is one of the key objectives of the double-diffusive convection theory. Therefore, the utility of any reduced-dynamics double-diffusive model is ultimately determined by its ability to accurately evaluate (4.4).

To that end, in figure 6 we plot the mean values of (F_T, F_S, F_ρ, E) for a series of SMF runs performed with $(Pr, \tau, R_\rho) = (7, 0.01, 2)$ in which we systematically vary the resolution (δ). These simulations were performed with $N \equiv N_x = N_z = 64$, 96, 128 192,
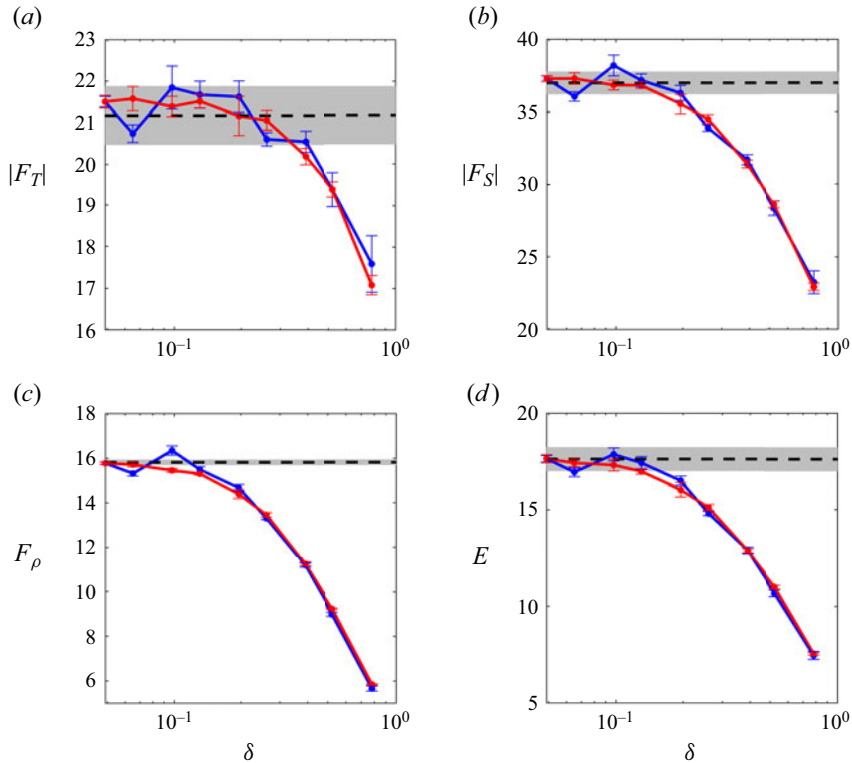
Figure 6. Convergence analysis of the SMF model. The magnitudes of heat flux (*a*), salt flux (*b*), density flux (*c*) and energy (*d*) are plotted as functions of the resolution (δ). The simulations performed with the adaptive-*C* model are shown in blue and the constant-*C* model ($C = 0.1$) are indicated by the red curves. The dashed lines represent fully resolved DNS. The error bars reflect the uncertainties in the estimates of averages associated with the finite length of records for the SMF model. The shaded regions represent the analogous uncertainties for the DNS model.

256, 384, 512, 768 and 1024. We average the diagnostic quantities (4.4) in time over the quasi-equilibrium interval $100 < t < 1000$. Both adaptive-*C* and constant-*C* models are presented, along with the estimates based on the fully resolved DNS in figure 1. The adaptive-*C* experiments indicate the optimal values of the Smagorinsky coefficient do not exceed $C = 0.11$ regardless of the resolution. This finding guides the calibration of the fixed-*C* model, and $C = 0.1$ is used for the latter. The adaptive-*C* and fixed-*C* experiments are mutually consistent, revealing the monotonic convergence of quantities (4.4) to their DNS-based counterparts with decreasing δ.

While the SMF model substantially underestimates the integral quantities (4.4) for $N = 64$ and $N = 96$, its accuracy improves considerably in better-resolved runs. For instance, the differences between the SMF-based and DNS-based estimates of the salinity (temperature) flux reduce to less than 15% (5%) for $N \geq 128$ ($\delta \leq 0.39$). It should be noted that all quantities in (4.4) are characterized by substantial temporal variability. The uncertainty of our estimates of the temporal averages that can be attributed to this variability is assessed as follows. We compute a series of averages over smaller intervals ($\Delta t_{av} = 450$) within the equilibrium range $100 < t < 1000$ and then use the root-mean-square variability of the resulting estimates as a measure of error. The length-of-record uncertainty, which is also indicated in figure 6, turns out to be
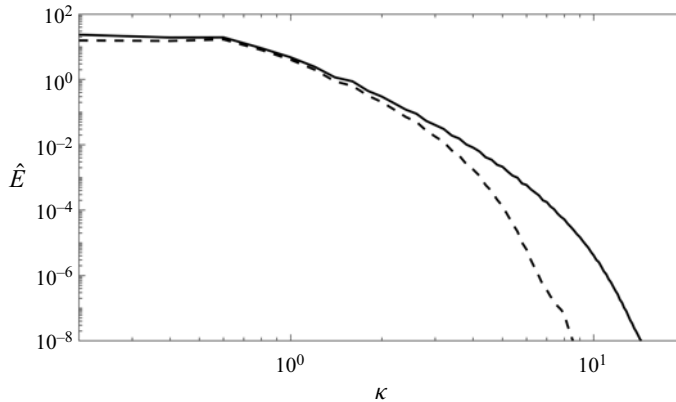
Figure 7. The spectrum of kinetic energy for the fully resolved DNS (solid curve) and its SMF counterpart (dashed curve).

particularly large for the temperature fluxes. The estimates of F_T offered by the SMF model for $N \geq 256$ ($\delta \leq 0.195$) are statistically undistinguishable from their DNS-based counterparts.

Figure 7 presents the spectra of kinetic energy $\hat{E}(\kappa)$, where

$$E = \int \hat{E}(\kappa)\,\mathrm{d}\kappa. \tag{4.6}$$

The energy spectra are shown for the fully resolved simulation (figure 1) and its SMF counterpart performed with $N = 128$ (figure 5). The two spectra are mutually consistent for relatively low wavenumbers ($\kappa \lesssim 3$) but the SMF model appears to be more aggressive in suppressing high-wavenumber harmonics. It should be emphasized, however, that both models reveal the lack of any substantial velocity patterns on scales that are much less than the typical size of salt fingers ($\kappa \gtrsim 10$). These diagnostics support the principal tenet of the SMF model, which assumes that sub-microscale dynamics of velocity and temperature is inconsequential.

Figure 8 presents the convergence analysis for the low-diffusivity case with $\tau = 5 \times 10^{-4}$. Once again, we observe the rapid reduction in the model error with decreasing δ. For $N = 196$, the SMF experiments underestimate the vertical T and S transport by less than 2% and 12%, respectively. The errors of such magnitude can be tolerated in most double-diffusive applications, particularly considering the dramatic gain in efficiency relative to the corresponding fully resolved DNS – recall, for instance, that the experiment in figure 2(c,d) was performed with $N = 4096$. It is also possible that the relatively poor performance of the SMF model for $N = 64$ and $N = 96$ is partially caused by the incompletely resolved temperature and momentum fields, rather than by the deficiencies of the subgrid closure itself.

6. Validation: 3-D simulations

Our next step is the validation of the SMF model in three dimensions. It is well known that cross-scale energy transport is fundamentally different in 2-D and 3-D turbulence (e.g. Kraichnan 1967). Therefore, despite its impressive performance in two dimensions, the ability of the SMF model to represent 3-D systems should not be taken for granted.
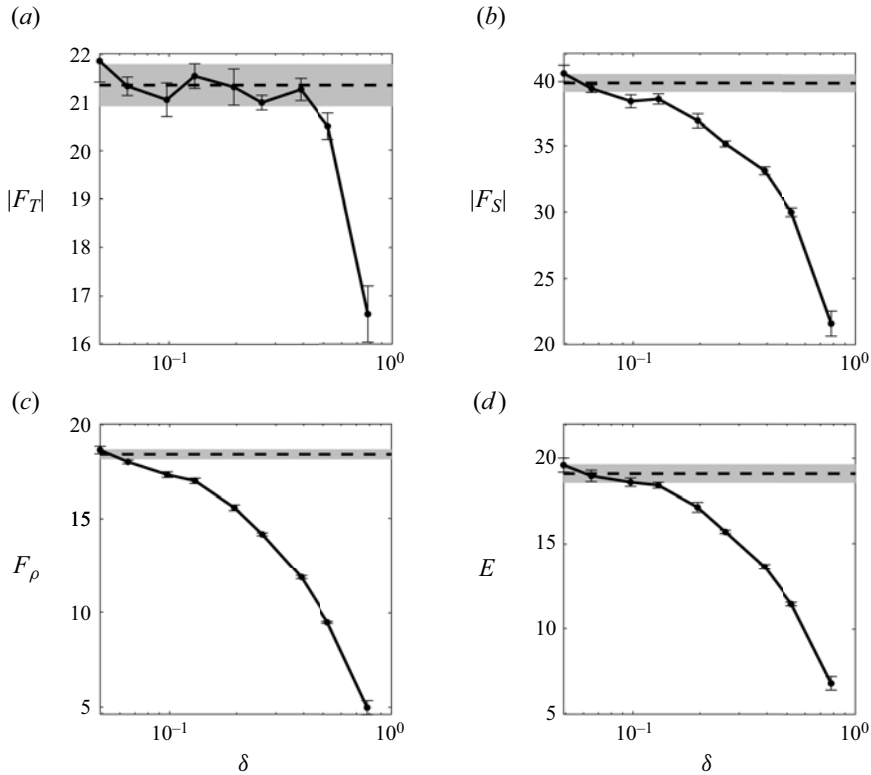
Figure 8. The same as in figure 6 but for the low-diffusivity SMF experiments performed with $\tau = 5 \times 10^{-4}$. All simulations employ the adaptive-C closure.
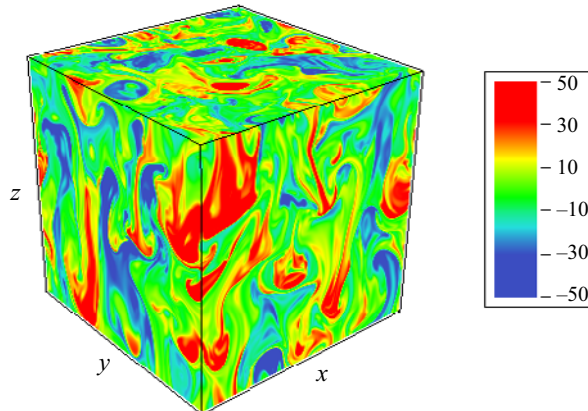

Figure 9. The 3-D DNS performed with $(Pr, \tau, R_\rho) = (7, 0.01, 2)$. Presented is the instantaneous pattern of salinity at $t = 100$.

To establish a baseline for the validation, we perform a set of 3-D DNS. The size of the computational domain used in these simulations is $L_x \times L_y \times L_z = 30 \times 30 \times 30$, and it is resolved by $(N_x, N_y, N_z) = (800, 800, 800)$ grid points. Our first example (figures 9 and 10) is a DNS performed with $(Pr, \tau, R_\rho) = (7, 0.01, 2)$. Figure 9 presents a typical salinity field realized in the quasi-equilibrated evolutionary stage. In agreement with earlier studies (e.g. Radko & Smith 2012; Radko *et al.* 2015), 3-D salt fingers (figure 9)
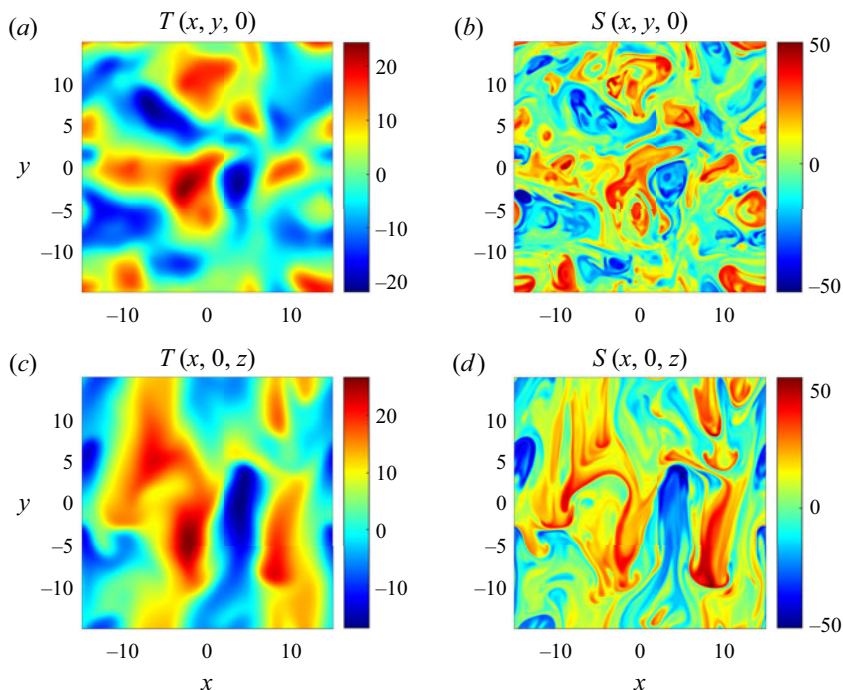
Figure 10. Horizontal (*a,b*) and vertical (*c,d*) sections of temperature (*a,c*) and salinity (*b,d*) for the state in figure 9.

proved to be structurally similar to – but more intense than – their 2-D counterparts (figure 1). In figure 10, we plot horizontal and vertical cross-sections of temperature (*a,c*) and salinity (*b,d*) for the state in figure 9 taken across the centre of the computational domain. The (*x,z*) sections are characterized by the emergence of vertically elongated filaments, whereas the (*x,y*) patterns are statistically isotropic. Particularly relevant for our discussion is the abundance of sub-microscale features in both horizontal and vertical sections of salinity – features that are not reflected in the corresponding temperature fields.

To determine whether the DNS results (figures 9 and 10) can be adequately reproduced using the SMF model, we turn to simulations based on (4.2) with the adaptive-*C* closure. The mesh used for these runs is systematically refined by increasing the number of grid points in each direction: $N \equiv N_x = N_y = N_z = 64$, 96, 128 192, 256 and 384. Other parameters match those of the simulation in figure 9. Figures 11 and 12 present the SMF experiment performed with $N = 128$. Despite the dramatic difference in resolution, the finger-scale processes in figures 9 and 11 are structurally similar. The fully resolved DNS (figure 9) exhibits a wider range of salinity scales, but the typical magnitudes of salinity perturbations in the two simulations are consistent. The comparison of the *T*–*S* cross-sections in figures 10 and 12 carries the same message. The SMF model filters the sub-microscale components of salinity in a way that does not significantly alter the dynamics of larger scales of motion.

To be more quantitative in assessing the performance of the SMF model, we now examine its convergence. In figure 13, we plot the quasi-equilibrium values of (F_T, F_S, F_ρ, E) as functions of the resolution (δ) along with the corresponding prediction based on the fully resolved simulation (figures 9 and 10). These diagnostics reveal an impressive skill of the SMF model in predicting key integral characteristics of the
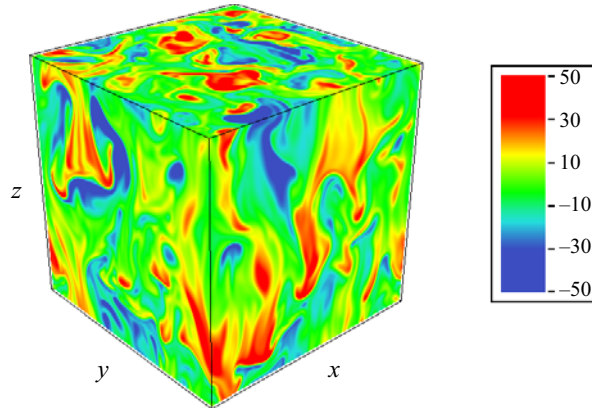
Figure 11. The SMF experiment performed with $N = 128$ and $(Pr, \tau, R_\rho) = (7, 0.01, 2)$. Presented is an instantaneous pattern of salinity at $t = 100$. Note the qualitative similarity of the flow field to its fully resolved counterpart in figure 9.
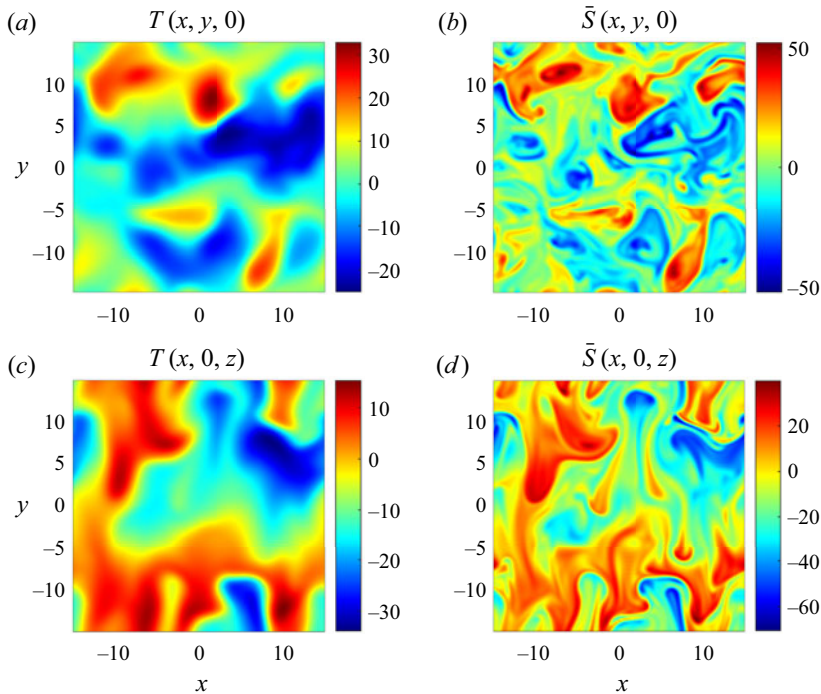

Figure 12. Horizontal (a,b) and vertical (c,d) sections of temperature (a,c) and salinity (b,d) for the state in figure 11.

flow field. In all cases, the model error rapidly decreases with increasing resolution. Particularly impressive is the model performance for very low N. The errors of the predicted salt and temperature fluxes for the smallest grid with $N = 64$ ($\delta = 0.469$) are only 4% and 20%, respectively. It is interesting to note that the estimates of salt fluxes by the SMF model are consistently better in three dimensions (figure 13) than in two dimensions (figure 6). For instance, the accuracy of 4% for F_S in two dimensions is attained only
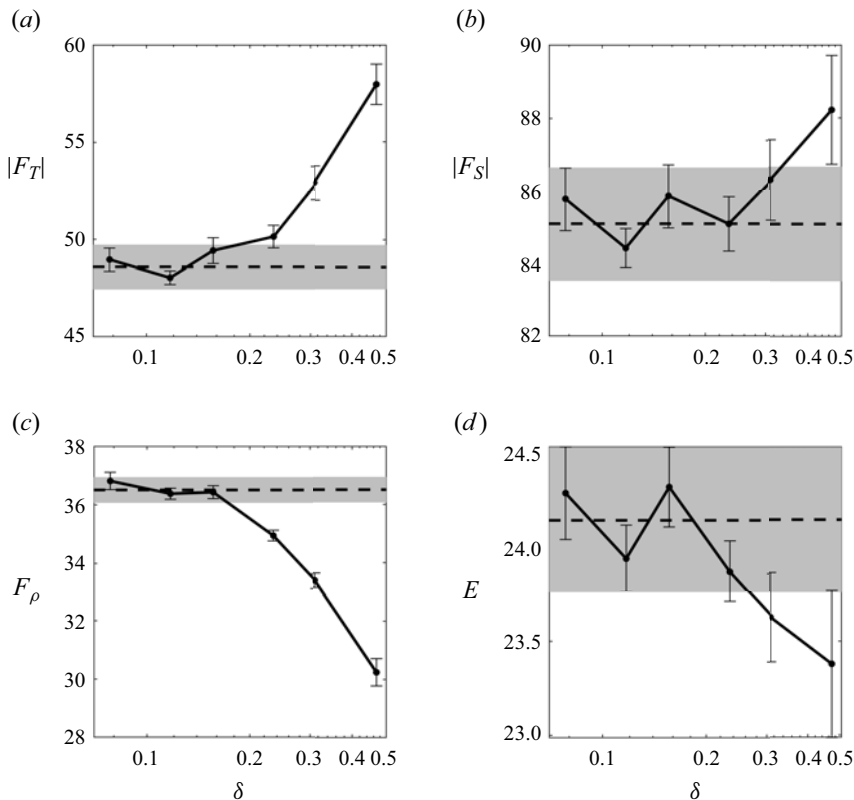
982 A25-16

Figure 13. Convergence analysis of the 3-D SMF model performed with $R_\rho = 2$. The magnitudes of heat flux (*a*), salt flux (*b*), density flux (*c*) and energy (*d*) are plotted as functions of the resolution (δ).

for $\delta \leq 0.2$ ($N \geq 256$). The superior performance of the SMF model in three dimensions can be attributed to the downscale (upscale) transfer of energy in 3-D (2-D) turbulence (Kraichnan 1967). The inverse 2-D cascade implies that inaccuracies in the representation of sub-microscale salinity patterns could spread upscale and contaminate larger scales of motion. On the other hand, the direct 3-D cascade effectively constrains the model errors to the high-wavenumber part of the spectrum.

Finally, to explore the relevant parameter space, we perform two additional convergence studies for $R_\rho = 1.5$ and $R_\rho = 3$, while keeping $(Pr, \tau) = (7, 0.01)$. The density ratio of $R_\rho = 1.5$ leads to some of the more intense salt fingering in the ocean, such as realized in the Caribbean Sea, whereas $R_\rho = 3$ represents its relatively mild form, more common in the Pacific thermocline. The results (figures 14 and 15) are consistent with our earlier findings (cf. figure 13). The key flow properties (4.4) systematically approach their DNS-based counterparts when δ is decreased. In the most violent regime (figure 14), the SMF model is slightly less accurate than in its less energetic counterparts (figures 13 and 15), particularly in terms of predicting the density flux. However, in all cases, adequate estimates are obtained even when the number of points in each dimension is less by an order of magnitude than demanded by fully resolved DNS. Considering the associated increase in the time step controlled by the CFL (Courant–Friedrichs–Lewy) condition, the computational savings brought by the 3-D SMF model are of the order of 10^4.
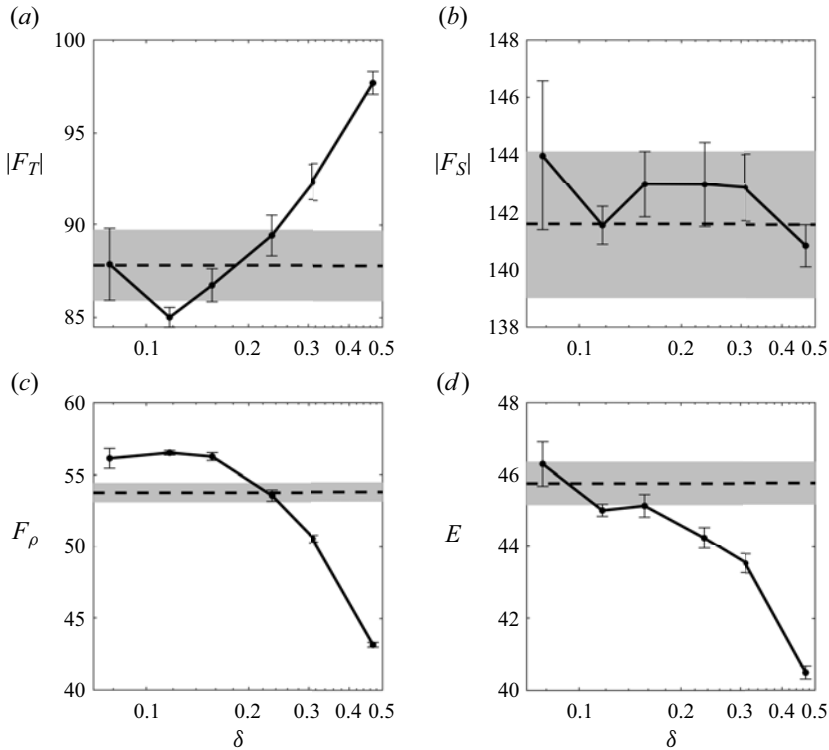
Figure 14. The same as in figure 13 but for the experiments performed with $R_\rho = 1.5$.

A pragmatic question can be raised at this point regarding resolution guidelines for the SMF model. Based on all simulations in this study, two-dimensional and three-dimensional, we suggest that the grid spacing of $\delta_{cr} = 0.2$ is sufficient to capture the key processes at play. This criterion is equivalent to resolving the nominal Stern (1960) finger scale $l = (k_T \upsilon / g\alpha A_T)^{1/4}$ by at least five grid points. Admittedly, our *ad hoc* recommendation is based on the Fourier spectral model and may require modification for other numerical algorithms.

7. Discussion

This study explores the sub-microscale dynamics of fingering convection. We are interested in flow features with scales that are much less than the typical size of individual salt fingers. On such scales, the slower diffusing property (salinity in the oceanographic context) develops narrow fronts that play a prominent role in the dissipation of the salinity variance. The emergence of these salinity structures stands in stark contrast with the lack of sub-microscale patterns of velocity and the faster diffusing density component (temperature in the ocean), which is attributed to the rapid molecular dissipation of heat and momentum. The very dissimilar evolution of salinity is not surprising, given that molecular viscosity and temperature diffusivity exceed the diffusivity of salt by two and three orders of magnitude, respectively. It is shown that the formation of sub-microscale salinity patterns is controlled by the finger-scale strain. Both shear and normal components of strain tend to systematically stretch and tighten salinity fronts until they are narrow enough to be affected by weak molecular dissipation of salt.
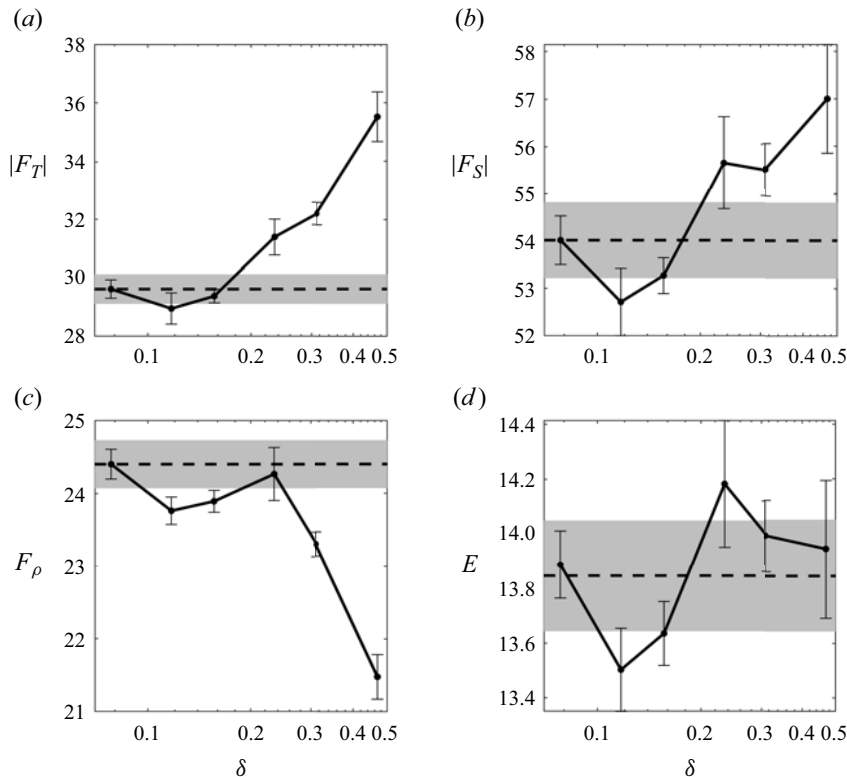
Figure 15. The same as in figures 13 and 14 but for the experiments performed with $R_\rho = 3$.

The spontaneous development of sub-microscale salinity patterns presents a major obstacle to numerical modelling of double-diffusive phenomena. The failure to represent these structures has catastrophic consequences for the stability and accuracy of models, rendering them largely unusable. At the same time, the requirement to fully resolve all relevant scales makes double-diffusive DNS prohibitively expensive. The computational cost can exceed that of the equivalent temperature-only simulations by three or four orders of magnitude, placing several double-diffusive problems beyond the reach of even the most advanced supercomputers.

Motivated by the principal limitation of the traditional DNS as a modelling tool for many double-diffusive problems, we develop a model of two-component flows that fully resolves velocity and temperature but parameterizes the subgrid transfer of salinity. Based on the analysis of sub-microscale dynamics (§ 3), we consider the strain-dependent subgrid closure for salinity. The proposed algorithm is reminiscent of the treatment of the momentum transfer in the pioneering model of Smagorinsky (1963). The convergence analysis indicates the proposed model (SMF) performs well for fingering convection in the oceanographically relevant regime. It produces representative flow patterns and accurate estimates of mixing even when the number of points in each dimension is less by an order of magnitude than required by DNS. It is interesting to note that the attempts (not shown) to implement explicit spectral cutoff filters for salinity have led to highly erratic model behaviour and were eventually abandoned. Such a contrast in terms of reliability and fidelity with the presented model is attributed to its robust, physics-based foundation. Of particular significance is the link between the salinity dissipation and the finger-scale

strain, exploited by the proposed algorithm. The connection between strain and dissipation is the crux of the classical theories of scalar transfer in turbulent systems (Batchelor 1959; Kraichnan 1974) and is shown here to control the dynamics of double-diffusive convection as well.

While the developments reported here appear to be highly promising, they should be viewed just as a first step in the search for the optimal SMF scheme. The first LES turbulence models inspired a multitude of enhancements in several branches of computational fluid dynamics – the efforts reviewed recently by Moser, Haering & Yalla (2021). By the same token, we hope that the presented algorithm will place the double-diffusive community on the path toward continuously evolving SMF modelling. The essential physics of sub-microscale processes and traditional turbulence problems are fundamentally different in many ways. As a result, the design of SMF models must be guided by principles that are not reflected in conventional LES algorithms. Nevertheless, such efforts will eventually make it possible to address grand-challenge problems in our field, such as the realistic modelling of thermohaline staircases and double-diffusive interleaving. The natural next step should involve the application of SMF models to diffusive convection problems, where cold and fresh water masses overly the relatively warm and salty ones.

Another major item on our wish list is the expansion of this analysis beyond the heat–salt systems. In this regard, we note that some double-diffusive applications are even more challenging computationally than the oceanic case (Schmitt 1983; Radko 2013). For instance, the diffusivity of silicate melt components can be extremely low ($\tau \sim 10^{-3}$–10^{-8}) and so is the compositional diffusivity in stars ($\tau \sim 10^{-6}$–10^{-8}). As a result, the disparity of dissipation scales of density components is dramatic, and the fully resolved DNS are not only computationally expensive but currently impossible. For such systems, SMF modelling may be the only resort in the foreseeable future.

Declaration of interests. The author reports no conflict of interest.

Author ORCIDs.
Timour Radko http://orcid.org/0000-0002-5682-280X.

Appendix A. The spectral analysis of sub-microscale salinity patterns

The purpose of the following analysis is twofold. We offer a transparent physical interpretation of the processes that lead to the formation of sub-microscale salinity fronts, clearly visible in double-diffusive DNS (e.g. figure 2d). Concurrently, we explore in greater detail the strain-based filtering algorithm (§ 4) and rationalize its ability to control grid-scale processes with only a minimal impact on larger scales of motion.

The key feature of sub-microscale processes in fingering convection is the dominant role of molecular viscosity. In the ocean, molecular viscosity exceeds the diffusivity of salt by three orders of magnitude. The typical values of the Schmidt number for mid-latitude thermocline are $Sc \equiv \upsilon/k_S \approx 900$. The disparity in molecular dissipation of momentum and salinity explains the stark contrast between the absence of velocity patterns in the sub-microscale range and the abundance of salinity structures. The typical Reynolds numbers based on the salinity dissipation scales are low ($Re \sim 10^{-2}$), which also points to viscous control of sub-microscale double-diffusive processes. The dynamics that we wish

to discuss represents an interesting example of a complex and highly disorganized low-Re system.

To capture the sub-microscale dynamics, we turn to the advection–diffusion salinity equation. In the interest of simplicity and dynamic transparency, the analysis is based on the 2-D formulation:

$$\frac{\partial S}{\partial t} + u\frac{\partial S}{\partial x} + w\frac{\partial S}{\partial z} + \frac{w}{R_\rho} = \tau\nabla^2 S. \tag{A1}$$

We focus on processes with lateral extent that are much less than the finger scale ($\Delta x, \Delta z \ll 1$). On such scales, the velocity field, which lacks sub-microscale variability, is approximated by linear patterns:

$$\left.\begin{array}{l} \bar{u} = U_0 + U_x x + U_z z, \\ \bar{w} = W_0 + W_x x + W_z z, \end{array}\right\} \tag{A2}$$

where $(U_0, U_x, U_z, W_0, W_x, W_z)$ are constants. The salinity field, on the other hand, varies on both small and large scales:

$$S = \bar{S} + S', \tag{A3}$$

where $\bar{S}$ and S' are the suitably defined large-scale and small-scale components. Subtracting (A1) and its small-scale average yields

$$\frac{\partial S'}{\partial t} + \bar{u}\frac{\partial S'}{\partial x} + \bar{w}\frac{\partial S'}{\partial z} = \tau\nabla^2 S'. \tag{A4}$$

Assuming Galilean invariance, we assign $U_0 = W_0 = 0$ without loss of generality. The incompressibility approximation demands that

$$U_x + W_z = 0. \tag{A5}$$

Given its linear character, the perturbation salinity equation (A4) naturally lends itself to the analysis based on the evolution of individual Fourier modes

$$S = \tilde{S}\exp(\mathrm{i}kx + \mathrm{i}mz). \tag{A6}$$

The net strain rate (s) consists of shear (s_s) and normal (s_n) components:

$$s = \sqrt{s_n^2 + s_s^2}, \quad s_n = \frac{\partial u}{\partial x} - \frac{\partial w}{\partial z}, \quad s_s = \frac{\partial w}{\partial x} + \frac{\partial u}{\partial z}, \tag{A7a–c}$$

and we find it instructive to consider their effects separately.

A.1. *Shear strain*

To illustrate the impact of shear strain on sub-microscale structures, we consider a flow pattern with $U_z > 0$ and $U_x = W_x = W_z = 0$ – the unbounded plane Couette model. In this case, $s = s_s = U_z$ and $s_n = 0$. Because of the z-dependence of the coefficient $\bar{u}$ in (A4), the traditional spectral stability analysis requires substantial modification (e.g. Knobloch 1984; Shepherd 1985; Radko 2019*b*,*c*). The linear solutions of the Couette system can still be represented by a superposition of the plane-wave components (A6), but with

time-dependent wavenumbers and amplitude. Combining (A4) and (A6), we arrive at the explicit expression for wavenumbers

$$\left.\begin{array}{l} k = k_0, \\ m = m_0 - sk_0 t, \end{array}\right\} \tag{A8}$$

and the ordinary differential equation for the amplitude

$$\frac{1}{\tilde{S}}\frac{\mathrm{d}\tilde{S}}{\mathrm{d}t} = -\tau(m^2 + k^2), \tag{A9}$$

where $(\tilde{S}_0, k_0, m_0)$ denote the initial amplitude and wavenumbers of the plane wave (A6). Equation (A8) shows that, even if the z-wavenumber is relatively small initially, it continually increases in time:

$$|m| \sim sk_0 t \quad \text{for } t \to \infty, \tag{A10}$$

which manifests itself in the formation of very narrow salinity fronts, clearly visible in simulations. If the diffusivity ratio is small ($\tau \to 0$), then (A9) implies that the amplitude remains relatively uniform in time:

$$\tilde{S} \sim \tilde{S}_0. \tag{A11}$$

Equations (A10) and (A11) characterize the evolution of all small-scale spectral salinity components. As a result, the salinity variance, which is produced by finger-scale instabilities, inexorably spreads to smaller and smaller scales, eventually reaching the grid scale δ. The accumulation of salinity variance at the highest resolved wavenumber $m_{cr} = \pi/\delta$ can have catastrophic consequences for the stability and accuracy of numerical models used for double-diffusive simulations.

In this context, it is interesting to determine how the proposed SMF closure (§ 4) affects the sub-microscale evolutionary dynamics. To that end, we replace the explicit diffusion term in (A4) with its Smagorinsky-type counterpart:

$$\frac{\partial S'}{\partial t} + \bar{u}\frac{\partial S'}{\partial x} + \bar{w}\frac{\partial S'}{\partial z} = -C\delta^4 \boldsymbol{\nabla} \cdot (s\,\boldsymbol{\nabla}(\nabla^2 S')). \tag{A12}$$

This modification does not affect the temporal variation of wavenumbers (A8), but the amplitude equation changes dramatically:

$$\frac{1}{\tilde{S}}\frac{\mathrm{d}\tilde{S}}{\mathrm{d}t} = -C\delta^4 s(m^2 + k^2)^2. \tag{A13}$$

Thus, as time progresses, the vertical wavelength of each plane Fourier mode continuously reduces, and so does its amplitude. It is of interest to estimate the amplitude ($\tilde{S}_{cr}$) of each mode at the stage ($t = t_{cr}$) when its vertical wavelength approaches the marginally resolved range ($m = m_{cr}$). We integrate (A13) over the interval $0 < t < t_{cr}$ and simplify the result by retaining only the leading-order component in the limit $\delta \to 0$ and assuming that C is an order-one quantity:

$$\ln\left(\frac{\tilde{S}_0}{\tilde{S}_{cr}}\right) \sim \frac{C\pi^5}{5k_0\delta} \gg 1. \tag{A14}$$

Thus, by the time the wavenumber of each mode reaches the critical value of $|m_{cr}| \gg |k_0|, |m_0|$, its amplitude is dramatically reduced. This finding explains why salinity variance does not accumulate at the grid scale in SMF experiments (§§ 5 and 6), which prevents numerical complications that plague under-resolved double-diffusive DNS.

A.2. *Normal strain*

To examine the evolution of sub-microscale salinity features in the flow dominated by normal strain, we consider $U_x = -W_z > 0$ and $U_z = W_x = 0$. In this case $s = s_n = 0.5U_x$ and $s_s = 0$. As in the case of shear strain, the solution of (A4) and (A12) are sought in terms of Fourier components with time-dependent wavenumbers. The counterpart of (A8) for normal strain takes form

$$\left. \begin{aligned} k &= k_0 \exp(-0.5st), \\ m &= m_0 \exp(0.5st). \end{aligned} \right\} \tag{A15}$$

Equation (A15) indicates that m continuously increases in time, even more rapidly than in shear strain. The variation in the amplitude due to molecular diffusion is still described by (A9). Hence, in the limit $\tau \to 0$, the amplitude remains largely unchanged. Inevitably, m reaches the critical level ($m = m_{cr}$) where it is no longer resolved by the numerical mesh. Because of its substantial amplitude, such accumulation of salinity variance at the grid scale compromises model's performance.

The central question that arises at this point is whether closure (A12) could prevent this chain of events and permit extended integrations of double-diffusive systems. In normal-strain-dominated flows, the variation in amplitude is still described by (A13), which we combine with (A15) and integrate in time over the interval $0 < t < t_{cr}$. The result is simplified by considering its leading-order component in the limit $\delta \to 0$:

$$\ln\left(\frac{\tilde{S}_0}{\tilde{S}_{cr}}\right) \sim \frac{\pi^4 C}{2}. \tag{A16}$$

Thus, the Smagorinsky-type closure can effectively suppress the magnitudes of all harmonics, regardless of the strain magnitude. For $C = 0.1$ used in constant-C simulations (§ 5), (A16) implies that the amplitude of harmonics in normal strain reduces by a factor of $\tilde{S}_0/\tilde{S}_{cr} \sim 130$, which proves to be sufficient to control the grid-scale processes without substantial contamination of larger scales of salinity.

It should be emphasized that both (A14) and (A16) – the expressions that quantify filtering of grid-scale components of salinity in shear-strain and normal-strain-dominated flows – do not depend on any characteristics background flow field. We credit this property for the universal applicability and impressive performance of the Smagorinsky-type closure (4.2).

REFERENCES

BATCHELOR, G.K. 1959 Small-scale variation of convected quantities like temperature in turbulent fluid. Part 1. General discussion and the case of small conductivity. *J. Fluid Mech.* **5**, 113–133.

BROWN, J. & RADKO, T. 2022 Disruption of Arctic staircases by shear. *Geophys. Res. Lett.* **49**, e2022GL100605.

BROWN, J., & RADKO, T. 2024 Patterns, transport, and anisotropy of salt fingers in shear. *J. Phys. Oceanogr.* (in press). https://doi.org/10.1175/JPO-D-23-0049.1.

DILLON, T.M. & CALDWELL, D.R. 1980 Batchelor spectrum and dissipation in the upper ocean. *J. Geophys. Res.* **85**, 1910–1916.

GARAUD, P. 2018 Double-diffusive convection at low Prandtl number. *Annu. Rev. Fluid Mech.* **50**, 275–298.

GUTHRIE, J.D., FER, I. & MORISON, J. 2015 Observational validation of the diffusive convection flux laws in the Amundsen Basin, Arctic Ocean. *J. Geophys. Res. Oceans* **120**, 7880–7896.

HIERONYMUS, M. & CARPENTER, J.R. 2016 Energy and variance budgets of a diffusive staircase with implications for heat flux scaling. *J. Phys. Oceanogr.* **46**, 2553–2569.

KELLEY, D.E., FERNANDO, H.J.S., GARGETT, A.E., TANNY, J. & OZSOY, E. 2003 The diffusive regime of double-diffusive convection. *Prog. Oceanogr.* **56**, 461–481.

KHANI, S. & WAITE, M.L. 2015 Large eddy simulations of stratified turbulence: the dynamic Smagorinsky model. *J. Fluid Mech.* **773**, 327–344.

KIMURA, S., SMYTH, W. & KUNZE, E. 2011 Turbulence in a sheared, salt-fingering-favorable environment: anisotropy and effective diffusivities. *J. Phys. Oceanogr.* **41**, 1144–1159.

KIMURA, S. & SMYTH, W.D. 2007 Direct numerical simulation of salt sheets and turbulence in a double-diffusive shear layer. *Geophys. Res. Lett.* **34**, L21610.

KNOBLOCH, E. 1984 On the stability of stratified plane Couette flow. *Geophys. Astrophys. Fluid Dyn.* **29**, 105–116.

KRAICHNAN, R.H. 1967 Inertial ranges in two-dimensional turbulence. *Phys. Fluids* **10**, 1417–1423.

KRAICHNAN, R.H. 1974 Convection of a passive scalar by a quasi-uniform random straining field. *J. Fluid Mech.* **64**, 737–732.

LINDEN, P.F. 1974 Salt fingers in a steady shear flow. *Geophys. Fluid Dyn.* **6**, 1–27.

MA, Y. & PELTIER, W.R. 2021 Parametrization of irreversible diapycnal diffusivity in salt-fingering turbulence using DNS. *J. Fluid Mech.* **911**, A9.

MOSER, R.D., HAERING, S.W. & YALLA, G.R. 2021 Statistical properties of subgrid-scale turbulence models. *Annu. Rev. Fluid Mech.* **53**, 255–286.

OAKEY, N.S. 1982 Determination of the rate of dissipation of turbulent energy from simultaneous temperature and velocity shear microstructure measurements. *J. Phys. Oceanogr.* **12**, 256–271.

OSBORN, T.R. & COX, C.S. 1972 Oceanic fine structure. *Geophys. Fluid Dyn.* **3**, 321–345.

OUILLON, R., EDEL, P., GARAUD, P. & MEIBURG, E. 2020 Settling-driven large-scale instabilities in double-diffusive convection. *J. Fluid Mech.* **901**, A12.

RADKO, T. 2008 The double-diffusive modon. *J. Fluid Mech.* **609**, 59–85.

RADKO, T. 2013 *Double-Diffusive Convection*. Cambridge University Press.

RADKO, T., BALL, J., COLOSI, J. & FLANAGAN, J. 2015 Double-diffusive convection in a stochastic shear. *J. Phys. Oceanogr.* **45**, 3155–3167.

RADKO, T. 2019*a* Thermohaline layering on the microscale. *J. Fluid Mech.* **862**, 672–695.

RADKO, T. 2019*b* Thermohaline-shear instability. *Geophys. Res. Lett.* **46**, 822–832.

RADKO, T. 2019*c* Instabilities of a time-dependent shear flow. *J. Phys. Oceanogr.* **49**, 2377–2392.

RADKO, T. & SISTI, C. 2017 Life and demise of intra-thermocline mesoscale vortices. *J. Phys. Oceanogr.* **47**, 3087–3103.

RADKO, T. & SMITH, D.P. 2012 Equilibrium transport in double-diffusive convection. *J. Fluid Mech.* **692**, 5–27.

RUDDICK, B. & KERR, O. 2003 Oceanic thermohaline intrusions: theory. *Prog. Oceanogr.* **56**, 483–497.

RUDDICK, B. & RICHARDS, K. 2003 Oceanic thermohaline intrusions: observations. *Prog. Oceanogr.* **56**, 499–527.

SCHMITT, R.W. 1983 The characteristics of salt fingers in a variety of fluid systems, including stellar interiors, liquid metals, oceans, and magmas. *Phys. Fluids* **26**, 2373–2377.

SCHMITT, R.W. 1994 Double diffusion in oceanography. *Annu. Rev. Fluid Mech.* **26**, 255–285.

SCHMITT, R.W., LEDWELL, J.R., MONTGOMERY, E.T., POLZIN, K.L. & TOOLE, J.M. 2005 Enhanced diapycnal mixing by salt fingers in the thermocline of the tropical Atlantic. *Science* **308**, 685–688.

SHEPHERD, T.G. 1985 Time development of small disturbances to plane Couette flow. *J. Atmos. Sci.* **42**, 1868–1872.

SIMEONOV, J. & STERN, M.E. 2004 Double-diffusive intrusions on a finite-width thermohaline front. *J. Phys. Oceanogr.* **34**, 1724–1740.

SMAGORINSKY, J. 1963 General circulation experiments with the primitive equations. Part I. The basic experiment. *Mon. Weath. Rev.* **91**, 99–164.

SMYTH, W.D. & KIMURA, S. 2011 Mixing in a moderately sheared salt-fingering layer. *J. Phys. Oceanogr.* **41**, 1364–1384.

STELLMACH, S., TRAXLER, A., GARAUD, P., BRUMMELL, N. & RADKO, T. 2011 Dynamics of fingering convection II: the formation of thermohaline staircases. *J. Fluid Mech.* **677**, 554–571.

STERN, M.E. 1960 The 'salt-fountain' and thermohaline convection. *Tellus* **12**, 172–175.

STERN, M.E. 1967 Lateral mixing of water masses. *Deep Sea Res.* **14**, 747–753.

STERN, M.E. 1969 Collective instability of salt fingers. *J. Fluid Mech.* **35**, 209–218.

STERN, M.E., RADKO, T. & SIMEONOV, J. 2001 3D salt fingers in an unbounded thermocline with application to the Central Ocean. *J. Mar. Res.* **59**, 355–390.

STERN, M.E. & SIMEONOV, J. 2002 Internal wave overturns produced by salt fingers. *J. Phys. Oceanogr.* **32**, 3638–3656.

STERN, M.E. & TURNER, J.S. 1969 Salt fingers and convective layers. *Deep-Sea Res.* **16**, 497–511.

TURNER, J.S. 1985 Multicomponent convection. *Annu. Rev. Fluid Mech.* **17**, 11–44.

YANG, Y., CHEN, W., VERZICCO, R. & LOHSE, D. 2020 Multiple states and transport properties of double-diffusive convection turbulence. *Proc. Natl Acad. Sci.* **117**, 14676–14681.

YANG, Y., VERZICCO, R. & LOHSE, D. 2016 Scaling laws and flow structures of double diffusive convection in the finger regime. *J. Fluid Mech.* **802**, 667–689.

YOU, Y. 2002 A global ocean climatological atlas of the Turner angle: implications for double-diffusion and water mass structure. *Deep-Sea Res.* **49**, 2075–2093.